ACS APPLIED MATERIALS & INTERFACES

www.acsami.org

Research Article

Deep Learning-Accelerated Designs of Tunable Magneto-Mechanical Metamaterials

Chunping Ma, Yilong Chang, Shuai Wu, and Ruike Renee Zhao*

Cite This: https://doi.org/10.1021/acsami.2c09052

Read Online

ACCESS | Metrics & More | Article Recommendations | Supporting Information

ABSTRACT: Metamaterials are artificially structured materials with unusual properties, such as negative Poisson's ratio, acoustic band gap, and energy absorption. However, metamaterials made of conventional materials lack tunability after fabrication. Thus, active metamaterials using magneto-mechanical actuation for untethered, fast, and reversible shape configurations are developed to tune the mechanical response and property of metamaterials. Although the magneto-mechanical metamaterials have shown promising capabilities in tunable mechanical stiffness, acoustic band gaps, and electromagnetic behaviors, the existing demonstrations rely on the forward design methods based on experience or simulations, by which the metamaterial properties are revealed only after the design. Considering the massive design space due to the material and structural programmability, a robust inverse design strategy is desired to create the magneto-mechanical metamaterials with preferred tunable properties. In this work, we develop an inverse design framework where a deep residual network replaces the conventional finite-element analysis for acceleration, realizing metamaterials with predetermined global strains under magnetic actuations. For validation, a direct-ink-writing printing method of the magnetic soft materials is adopted to fabricate the designed complex metamaterials. The deep learning-accelerated design framework opens avenues for the designs of magneto-mechanical metamaterials and other active metamaterials with target mechanical, acoustic, thermal, and electromagnetic properties.

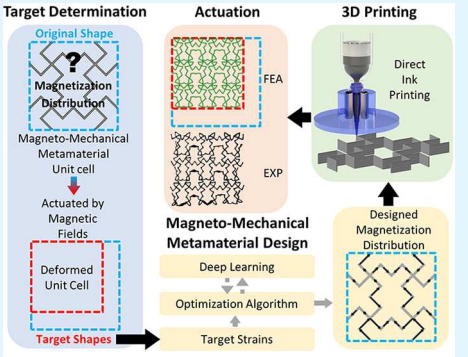

KEYWORDS: *magnetic soft materials, mechanical metamaterials, deep learning, ResNet, optimization*

INTRODUCTION

Metamaterials are artificially structured materials with carefully designed geometries, demonstrating unusual behaviors and properties, such as negative Poisson's ratio,[1,2] acoustic band gap,[3,4] energy absorption,[5,6] and electromagnetic wave manipulation.[7,8] Although mechanical metamaterials possess promising potentials, their property is encoded and unchangeable once the material is fabricated. Since metamaterial properties are mainly determined by their geometries, a direct way to enhance the tunability of the properties is to induce shape reconfiguration through deformation, such as buckling, by external mechanical loads.[3,9−11] Therefore, soft active materials are explored to construct active metamaterials as they are capable of providing large deformation upon external stimuli, including heat,[12−14] light,[15,16] and magnetic fields,[17,18] enabling contactless and advanced control.

Among varieties of soft active materials, the magnetic soft materials (MSMs) composed of soft polymer matrices and embedded hard-magnetic particles show a strong potential in applications including morphing devices,[19] soft robotics,[20,21] biomedical devices,[22,23] and active metamaterials,[24−28] thanks to their abilities to generate untethered, fast, and reversible shape configurations. When actuated by external magnetic fields, the magnetic particles exert micro-torques on the soft matrix to align the composite magnetization with the direction of the external field, resulting in complex shape changes. A theoretical model and corresponding finite-element (FE) model were developed to better understand and predict the mechanical behaviors of MSMs,[29] and a direct-ink-writing (DIW) technique is developed for the 3D printing of MSMs with sophisticated geometry and magnetization distribution (M-distribution),[24] as shown in Figure 1a. A printing magnetic field reorients the polarities of the magnetic particles in the magnetized ink to the longitudinal direction of the nozzle, endowing the printed filament with a magnetization direction (M-direction) along the printing direction. Based on the DIW and FE techniques for MSMs, more complex magneto-mechanical metamaterials can be developed, enabling more advanced control of shape transformation for tunable properties.[28] However, the magneto-mechanical metamaterials still significantly rely on the forward design method based on experience or FE analysis (FEA), by

Received: May 20, 2022
Accepted: June 29, 2022

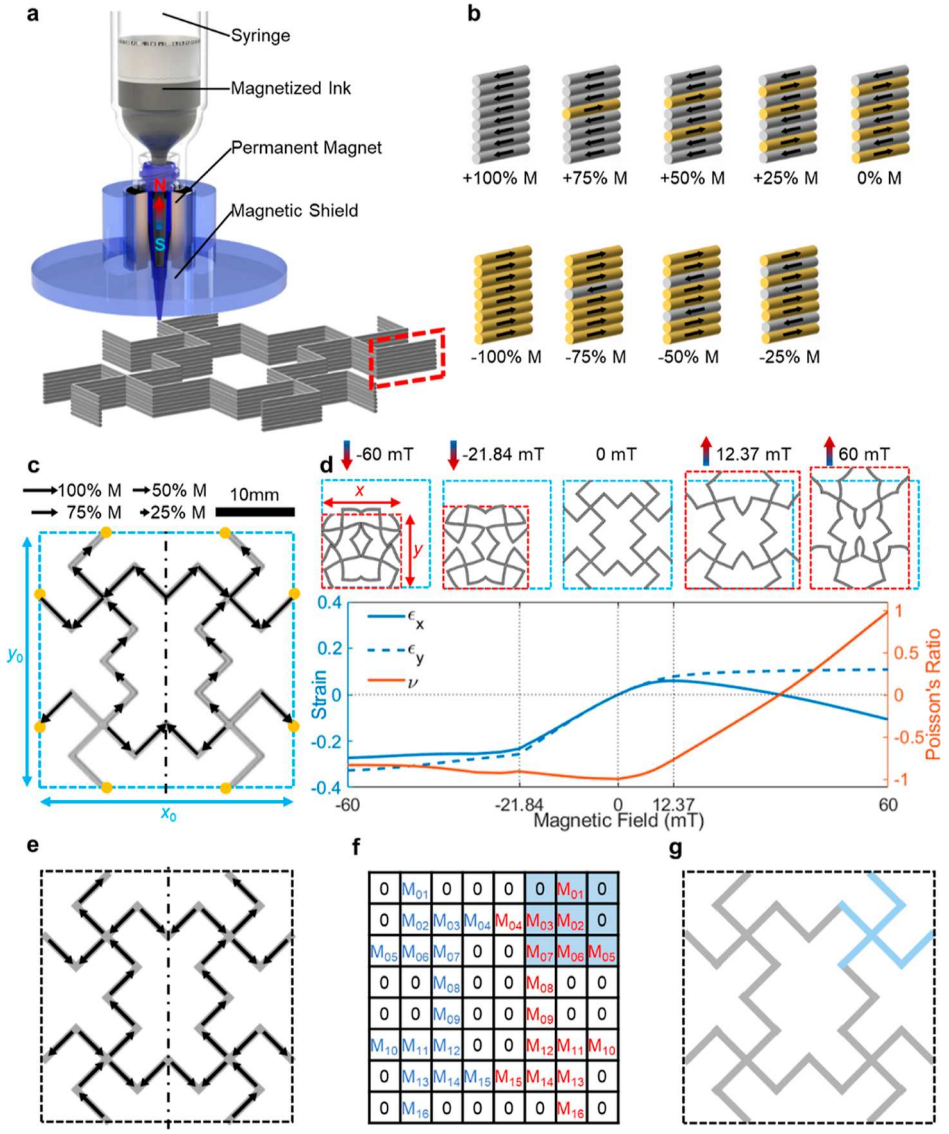

Figure 1. Programmable 3D printing and large design space of the magneto-mechanical metamaterials. (a) Schematics of the DIW of MSMs. (b) Schematics of the possible M-direction and M-magnitude for each segment. (c) M-distribution example of a unit cell. The yellow dots indicate the points determining the unit cell boundaries. (d) Deformation, global strains, and Poisson's ratio of the unit cell in (c) under changing magnetic field direction and intensity. (e) Definition of positive M-directions for each segment. (f) Numerical representation of the M-distribution using an 8-by-8 matrix, in which the blue area is under the operation of a 3 × 3 convolution kernel. (g) Unit cell geometry where the blue segments are under the operation of the 3 × 3 convolution kernel used in (f).

which the metamaterial properties are evaluated and revealed only after the design. Such methods become incompetent when the design targets are quantitatively specified, and the design space is large.

In this research, the goal is the on-demand design of magneto-mechanical metamaterials with target properties. To enhance the programmability of 3D-printed MSMs and extend the design space for the magneto-mechanical metamaterials, a voxel-encoding strategy[30] is adopted to obtain programmable magnetizations with different M-directions and M-magnitudes by tunning the arrangement of the printed filaments, which is schematically depicted in Figure 1b. In this way, one segment (highlighted by the red dash line box in Figure 1a) formed by eight layers of stacked filaments can achieve nine different effective magnetizations by simply altering the M-direction of the filaments. For a segment where the M-directions of all the eight filaments are toward the same direction, its effective magnetization magnitude is defined as +100% M. Then, by flipping the M-direction of one to eight filaments, we can obtain nine effective magnetization magnitudes from +100% M to −100% M with a uniform interval of 25% M. The more layers of filaments, the smaller the interval, and the finer the programmability will be.

Figure 1c shows the in-plane geometry of a magneto-mechanical metamaterial unit cell with an M-distribution example. Such unit cell geometry is composed of four chiral subunits with two orthogonal mirror symmetry axes. For each chiral subunit, a wide range of mechanical behavior including expansion, contraction, and rotation are allowed. Additionally, the structural mirror symmetry can effectively eliminate the global rigid-body rotation that is potentially induced by the deformation of the chiral subunit. There are 32 magnetic segments in one unit cell with only 16 of them being independent due to the *y*-axis mirror symmetry. The actuation

https://doi.org/10.1021/acsami.2c09052
ACS Appl. Mater. Interfaces XXXX, XXX, XXX−XXX

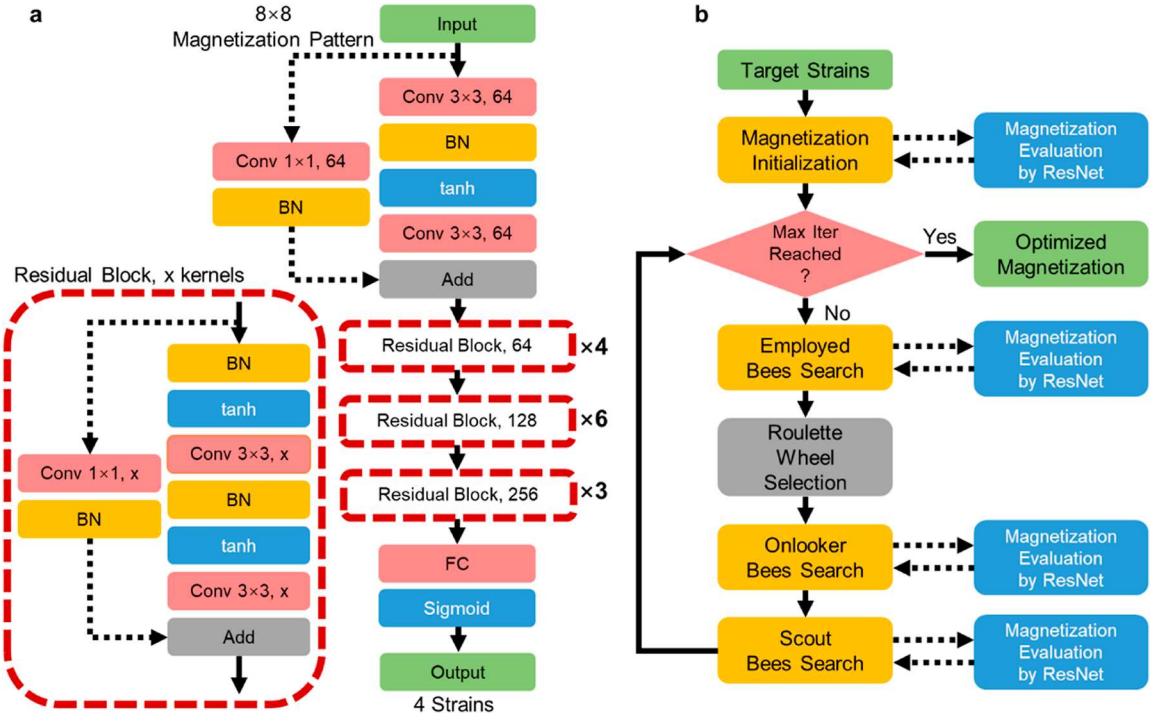

Figure 2. ResNet architecture and DABC-ResNet flowchart. (a) ResNet architecture. (b) DABC-ResNet flowchart.

magnetic field is always along the y-axis to eliminate the rigid-body rotation. The unit cell size is 32 mm × 32 mm, and the thickness and height of each magnetic segment are 0.57 and 3.0 mm, respectively, determined by the printing parameters used in the DIW system. The magnetization of each segment in the unit cell can have one of the nine combinations, as shown in Figure 1b, resulting in $9^{16} \approx 1.85 \times 10^{15}$ possible M-distributions of the unit cell. To concisely characterize the deformation of the periodic unit cell under magnetic actuation, we choose the global strains ε_x and ε_y, calculated as $\varepsilon_x = (x - x_0)/x_0$ and $\varepsilon_y = (y - y_0)/y_0$ where x_0, y_0, and x, y are the side lengths of the undeformed and the deformed unit cell. Four strains are obtained when an upward and a downward magnetic field with the same magnitude are applied. Although varying the magnitude of magnetic fields easily changes the deformation intensity of the metamaterial (Figure 1d), it cannot maintain the same Poison's ratio, making the global strain evolution in both directions nonlinear and highly unpredictable. Therefore, in this work, we focus on exploring the design space mainly contributed from the M-distribution, which provides determinacy for controllable strains.

Now the inverse design problem can be stated as finding the optimal M-distributions by which the unit cell deforms to specific strains under certain external magnetic fields. Thanks to the advances in computational methods and devices, deep learning has provided a new methodology in the research of metamaterials to either effectively predict certain properties of the metamaterials[31−34] or to generate the metamaterial configurations satisfying target properties.[35−39] In this case, directly solving the design problem by deep learning leads to a multi-task and multi-class classification problem with 16 tasks of nine-class classification, which is tricky to handle. Our inverse design problem prefers an optimization method, which should possess a strong global search ability considering the vast number of possible M-distributions. Here, a discrete artificial bee colony (DABC) algorithm is employed to find the optimal M-distribution for the target strains, in which a deep residual network (ResNet) is trained to replace the time-consuming FEA to accelerate the optimization process. In this paper, Section 2 illustrates computational methods in detail. Section 3 demonstrates the ability and accuracy of the proposed design method through simulations and experiments. The joint force of deep learning and nature-inspired optimization enables the efficient and effective inverse design of magneto-mechanical metamaterials and paves the road for other active metamaterials with target mechanical, acoustic, thermal, and electromagnetic properties.

DESIGN FRAMEWORKS AND ALGORITHMS

Data Set Preparation. Data set preparation is one of the most time-consuming yet fundamental procedures for deep learning. The data type and quantity determine the selection of deep learning methods, and the data distribution and quality influence the performance of the trained deep learning model. In this paper, the data set is generated using the FE software ABAQUS with a user-defined element subroutine.[29] In this paper, periodic boundary conditions are applied to precisely predict the mechanical behavior of a large array. In the deep learning process, the magnetization of each segment in the unit cell should be numerically represented as the input. Therefore, the nine magnetization types, as shown in Figure 1b, are transformed to ±1, ±0.75, ±0.5, ±0.25, and 0 accordingly, in which the positive/negative signs indicate two opposite effective M-directions of the segment magnetization. The positive M-directions for each segment are defined in Figure 1e.

The deformation and behavior of the unit cell are determined by the magnetization of each segment and the interaction between the connected segments. Thus, it is beneficial to have a deep learning model that captures the interaction. A suitable option is the model based on convolutional neural networks, which endows stronger connections to the closer elements in a matrix-type input. To accurately reflect both the magnetization

https://doi.org/10.1021/acsami.2c09052
ACS Appl. Mater. Interfaces XXXX, XXX, XXX−XXX

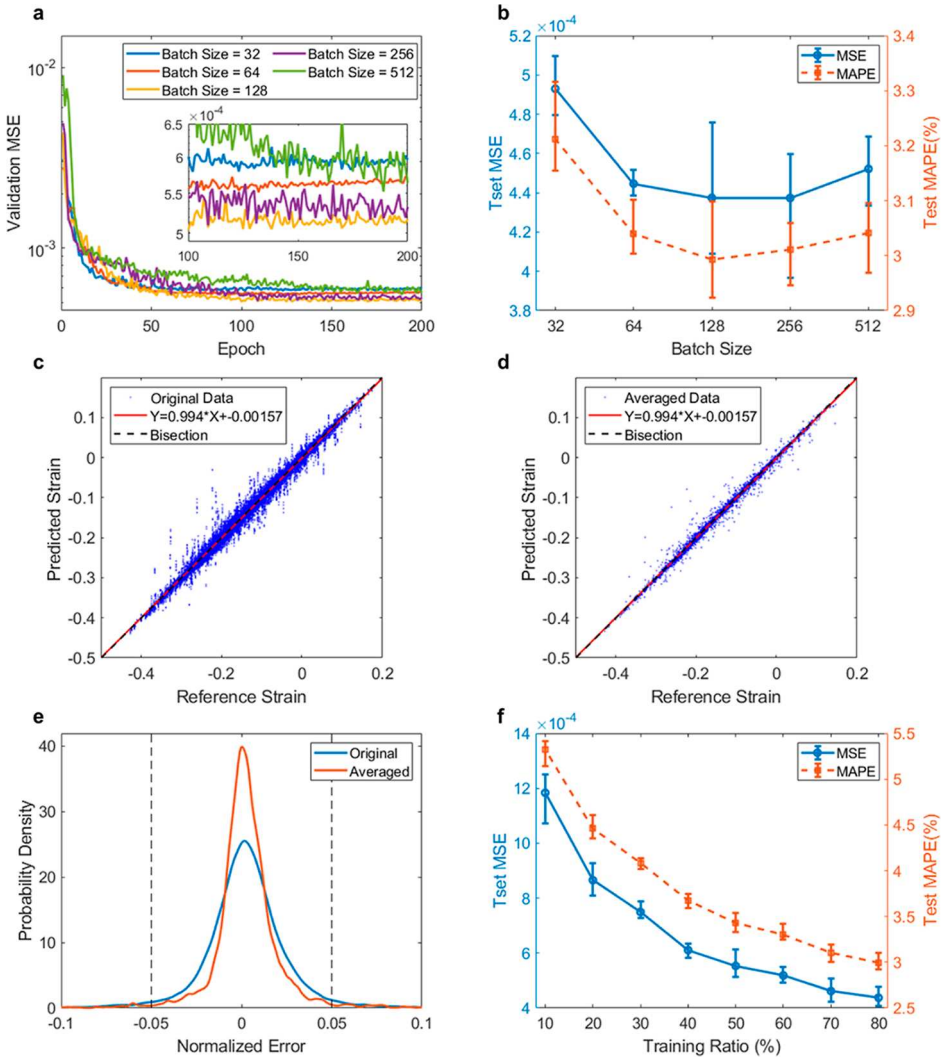

Figure 3. Model validation and performance of the ResNet. (a) Effect of batch numbers on MSE convergence evaluated on validation sets. (b) Effect of batch numbers on MSE and MAPE evaluated on test sets using averaged results. (c) Comparisons between predicted strains and reference strains. (d) Comparisons between averaged predicted strains and reference strains. (e) Comparison between the normalized error distributions before and after the average operation. (f) Effect of training ratios on MSE and MAPE evaluated on the sets.

of each segment and the actual interaction between the segments, the 32 magnetization values are arranged into an 8 × 8 matrix, as shown in Figure 1f, in which zero means no segment. The 3 × 3 area shaded in blue at the upper-right corner of the matrix represents a typical example of 3 × 3 convolution kernels applied to the matrix, and the corresponding segments are highlighted in Figure 1g.

Rearranging the orders and/or reversing the signs of the magnetization values in an M-distribution in certain ways results in another seven new M-distributions with the same strain values as the original M-distribution, as shown in Figure S1, which is used for data augmentation (see details in the Data Set Augmentation section of the Supporting Information). In this paper, we randomly generate 10,000 horizontally symmetric M-distributions and perform FEA to obtain metamaterial global strains, and the total number of M-distributions with known global strains in the data set reaches 10,000 × 8 = 80,000 after data augmentation.

ResNet. When using convolutional neural networks for the matrix-form inputs like our problem, it is common to add more convolutional layers to extract more information, but the performance can be degraded on both the training set and the validation set when adding extra layers to a feasible deep network.[40] The ResNet is proposed to solve this problem by introducing the identical mapping, which adds skip connections to allow the information to propagate between the shallow layer and the deeper layer.[41]

Figure 2a illustrates the architecture of the ResNet used in this paper. Major components include the convolutional (Conv) layer, batch normalization (BN) layer, and hyperbolic tangent activation function (tanh). The "3 × 3" is the size of the convolution kernel, and the following number indicates the number of channels. Each residual block, indicated by red dash boxes, is formed by two stacked BN-tanh-Conv blocks and a skip connection depicted by the black dash lines. The "×#" on the right side of each residual block represents that the block is repeated for # times. For all the repeated blocks with the same number of channels, the strides of all the Conv layers are equal to one except for the last Conv layer which has a stride of two, which halves the input matrix size and increases the representativeness of the extracted information. Meanwhile, the channel number in each residual block is doubled to

https://doi.org/10.1021/acsami.2c09052
ACS Appl. Mater. Interfaces XXXX, XXX, XXX−XXX

strengthen the extraction of the information from the previous block. The total number of convolutional layers in this model is 28. Note that the "same" padding is applied to all convolutional operations. Finally, to convert the captured features to strain values, a fully connected (FC) layer with a sigmoid activation function is added after the last residual block. Thanks to the identity mapping, it is usually not necessary to fine-tune the number of residual blocks. This model has 5,570,372 parameters in total, 5,559,748 of which are trainable.

DABC Algorithm. Considering the extensive design space of the magneto-mechanical metamaterials, a competent optimization method must possess outstanding global searchability, which excludes most gradient-based optimization methods since they can only guarantee local convergence. Typical gradient-free optimization methods such as annealing algorithms[42,43] and evolutionary/genetic algorithms[44−46] have been successfully applied in metamaterial designs. In this paper, an DABC algorithm[47−49] is applied to fulfill the design tasks of magneto-mechanical metamaterials considering the discrete nature of the magnetization representation. Another virtue of DABC is the simplicity in parameter settings, which only requires four parameters, viz., the population number N_p, the maximum iteration number N_{max}, the cycle limit for each solution N_{lim}, and the mutation rate r_m. In this paper, the parameters are set as N_p = 200, N_{max} = 300, N_{lim} = 100, and r_m = 0.3. DABC has three major phases, viz., the employed bee phase, the onlooker bee phase, and the scout bee phase, as shown by the flowchart in Figure 2b. The population with a size of N_p is formed by $N_p/2$ employed bees and $N_p/2$ onlooker bees. Before the optimization starts, N_p initial solutions of the M-distribution are randomly generated and evaluated, and the best half of the initial solutions (evaluated by eq S1e in the Supporting Information) are kept for the major phases (employed bee, the onlooker bee, and the scout bee). Note that all the magnetization evaluations in DABC are carried out using a trained ResNet to accelerate the optimization process. Detailed explanations and formulas can be found in the Supporting Information.

RESULTS AND DISCUSSION

ResNet Hyperparameter Determination and Prediction Accuracy. In this paper, the ResNet is constructed using Tensorflow,[50] trained by a stochastic gradient descent optimizer called Adam[51] with a learning rate of 0.001. The data set of 80,000 data from FEA is divided into three sets for training, validation, and test with a ratio of 8:1:1. Each training process takes 200 epochs. Because the different ranges of the four strains can cause training difficulty, each of the four strains is scaled to the range of [0.2, 0.8]. The loss function is defined as the mean squared error (MSE) between reference strains and predicted strains

$$\mathrm{MSE} = \frac{1}{4N}\sum_{i=1}^{N}\sum_{j=1}^{4}[\varepsilon_{ij}(\mathbf{M}_i) - \hat{\varepsilon}_{ij}(\mathbf{M}_i, \mathbf{W}, \mathbf{b})]^2 \quad (1)$$

where N is the number of data points in the test set, ε_{ij} is the jth reference strain value of the ith M-distribution $\mathbf{M}_i$ in the test set, and $\hat{\varepsilon}_{ij}$ is the jth predicted strain value of $\mathbf{M}_i$ with the trained weights $\mathbf{W}$ and biases $\mathbf{b}$. Meanwhile, the mean absolute percentage error (MAPE) is used as a more intuitional metric to evaluate the network performance

$$\mathrm{MAPE} = \frac{1}{4N}\sum_{i=1}^{N}\sum_{j=1}^{4}\left|\frac{\varepsilon_{ij}(\mathbf{M}_i) - \hat{\varepsilon}_{ij}(\mathbf{M}_i, \mathbf{W}, \mathbf{b})}{\varepsilon_{ij}(\mathbf{M}_i)}\right| \times 100\% \quad (2)$$

Note that MAPE only applies to the strains transferred to the range of [0.2, 0.8] because the original strains can have zeros values.

With the ResNet architecture, we train the network with a mini-batching strategy to overcome the local minima and boost the convergence rate.[52] We tested five different batch sizes increasing from 32 to 512 at a ratio of 2 for five times independently, and the data set is randomly shuffled each time. Figure 3a shows the average convergence plots of the validation loss evaluated by MSE, and the optimal batch size is 128. The computational device and time of ResNet are reported in the Supporting Information.

To further improve the prediction accuracy, an average operation is applied based on the knowledge from the data augmentation (see details in the Supporting Information). For the comparison of the performance among different batch sizes after the average operation, for each 200-epoch training process, we use the network from the epoch where the test MAPE takes the minimum as the final network to perform the average operation on the test set, and the results are summarized in Figure 3b, indicating that the optimal batch size is 128. Figure 3c visualizes the accuracy of the predicted strains yielded by the best ResNet using a batch size of 128, and the narrow band around the bisection line suggests a good performance. An even narrower band is observed in Figure 3d where the average operation is performed, proving the effectiveness of the average operation. See Figure S2 for the scatter plots of the strains on a certain axis and under a certain magnetic field direction.

Another way to evaluate the accuracy is by the probability density function (PDF) of the normalized error $\mathrm{NE}_{ij} = [\varepsilon_{ij}(\mathbf{M}_i) - \hat{\varepsilon}_{ij}(\mathbf{M}_i, \mathbf{W},\mathbf{b})]/\varepsilon_{ij}(\mathbf{M}_i)$, as plotted in Figure 3e. The averaged predictions are more accurate since their NE is more concentrated near zero. We calculate the probability P that the NE is within certain ranges for quantitative comparisons. For original predictions, $P(|\mathrm{NE}| < 0.05) = 0.9533$, $P(|\mathrm{NE}| < 0.1) = 0.9918$. For averaged predictions, $P(|\mathrm{NE}| < 0.05) = 0.9683$, $P(|\mathrm{NE}| < 0.1) = 0.9933$. The average operation improves $P(|\mathrm{NE}| < 0.05)$ by 1.5%.

For the data set size, though a larger data set is preferred, our ability to collect data is limited. Thus, it is important to estimate the data set size needed to obtain satisfying training results. Using the optimal batch size 128, we keep the test set as 10% of the whole data set, while gradually reducing the training ratio from 80 to 10% of the whole data set. The model is trained independently five times for each training ratio, and the statistical results are summarized in Figure 3f. Though there can still exist a small descending trend of MSE/MAPE if using larger training sets, the result from 80% is close to saturation.

Magneto-Mechanical Metamaterial Designs and Validations. In this section, we utilize seven types of target strains to demonstrate the design ability of the proposed DABC-ResNet design framework as well as the wide tunability of the magneto-mechanical metamaterials. Each type controls a certain combination of target strains. The features and corresponding figures of each type are summarized in Table 1. For each type, the strain behaviors under both magnetic field directions are controllable. The target strain can be zero, uniaxial (on X-axis or Y-axis), or biaxial, and the Poisson's ratio ($\nu = -\varepsilon_x/\varepsilon_y$) can be

https://doi.org/10.1021/acsami.2c09052
ACS Appl. Mater. Interfaces XXXX, XXX, XXX−XXX

Table 1. Summary of Seven Types of Target Strains

	under one magnetic field direction		under opposite magnetic field direction		
type	strain	Poisson's ratio ν	strain	Poisson's ratio ν	figures
A	*X*-axis uniaxial	$\nu = 0$	zero strain		Figures 4a and S3
B	*X*-axis uniaxial	$\nu = 0$	X-axis uniaxial	$\nu = 0$	Figures 4b and S4
C	*X*-axis uniaxial	$\nu = 0$	*Y*-axis uniaxial	$\nu = 0$	Figures 4c and S5
D	biaxial	$\nu < 0$	zero strain		Figures 4d and S6
E	*Y*-axis uniaxial	$\nu = 0$	biaxial	$\nu < 0$	Figures 6a,b and S7
F	biaxial	$\nu < 0$	biaxial	$\nu < 0$	Figures 6c,d and S8
G	biaxial	$\nu < 0$	biaxial	$\nu > 0$	Figures 6e,f and S9

negative, zero, or positive. FEA is performed to verify the resulting strains of all the designed M-distributions, and examples from Type A to Type D are 3D-printed for experimental validations.

Figure 4 shows four examples from Type A to Type D target strains, respectively. Type A (Figure 4a) focuses on the control of the uniaxial strain with zero Poisson's ratio under one magnetic field and zero strain under the opposite magnetic field. Type B (Figure 4b) aims at the control of the uniaxial strain on the same axis with zero Poisson's ratio under two opposite magnetic fields. Type C (Figure 4c) targets the control of the uniaxial strain on different axes with zero Poisson's ratio under two opposite magnetic fields. Type D (Figure 4d) is for the control of the biaxial strain with negative Poisson's ratio under one magnetic field and zero strain under the opposite magnetic field. Note that, based on the knowledge from the data augmentation (e.g., Figure S1a,b), using an arbitrary M-distribution can easily obtain a new M-distribution that has the same strain when under the opposite magnetic field.

For each example in Figure 4, the target strains, the strains predicted by DABC-ResNet, and the strains from the FEA of the designed M-distribution are summarized in the table on the left side, in which the strain values under the downward and upward magnetic fields are shaded by blue and orange, respectively. On the right side of the table is the vector map of the designed M-distribution, followed by the deformation comparisons on the unit cell level between FEA and experimental results where the deformations under downward and upward magnetic fields are marked by blue and orange backgrounds, respectively. The target Poisson's ratio ν is also noted above the deformation. It

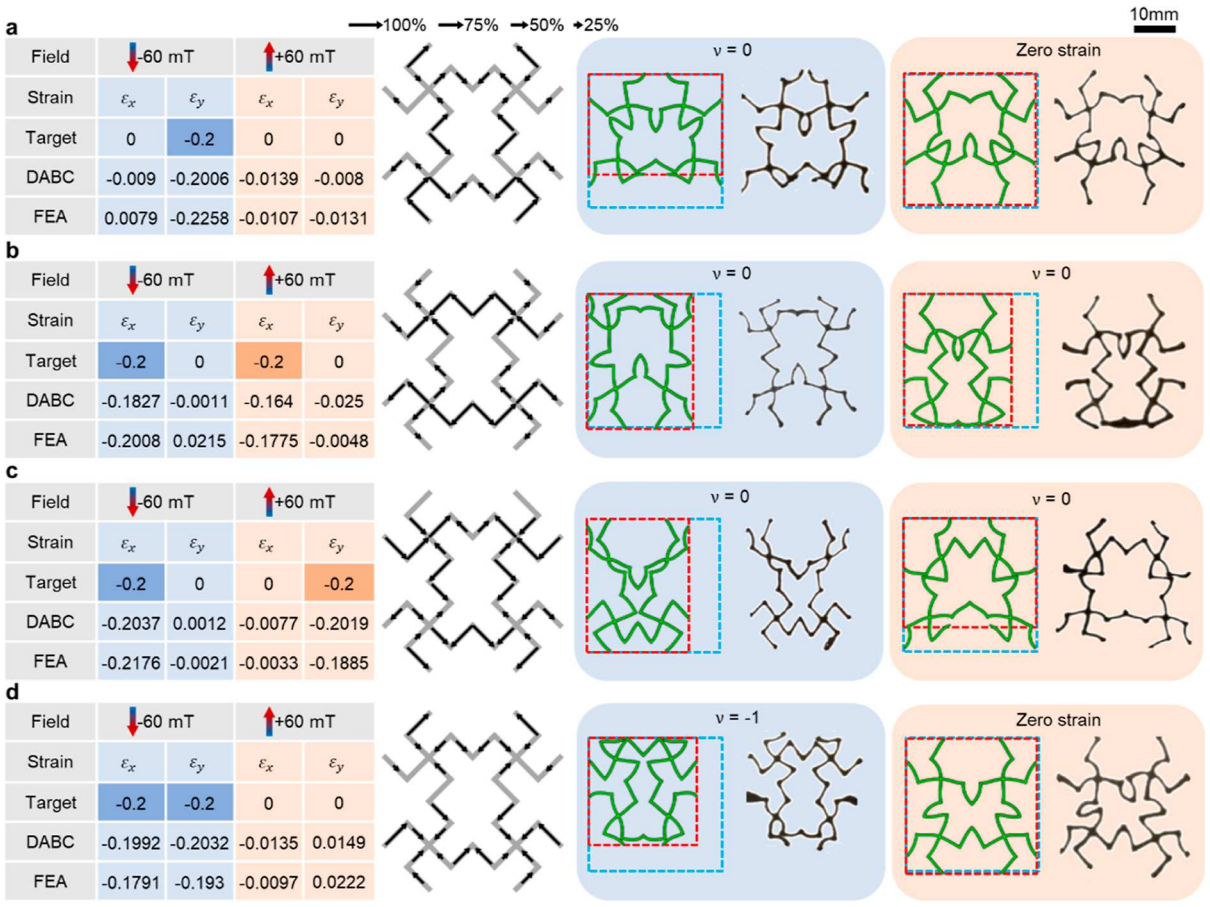

Figure 4. Examples of designed M-distributions, FEA results, and experimental validations from Type A to Type D of target strains for deformation control. (a) Example from Type A for the control of the uniaxial strain with zero Poisson's ratio under one magnetic field and zero strain under the opposite magnetic field. (b) Example from Type B for the control of the uniaxial strain with zero Poisson's ratio under two opposite magnetic fields on the same axis. (c) Example from Type C for the control of the uniaxial strain with zero Poisson's ratio under two opposite magnetic fields on different axes. (d) Example from Type D for the control of the biaxial strain with negative Poisson's ratio under one magnetic field and zero strain under the opposite magnetic field.

https://doi.org/10.1021/acsami.2c09052
ACS Appl. Mater. Interfaces XXXX, XXX, XXX−XXX

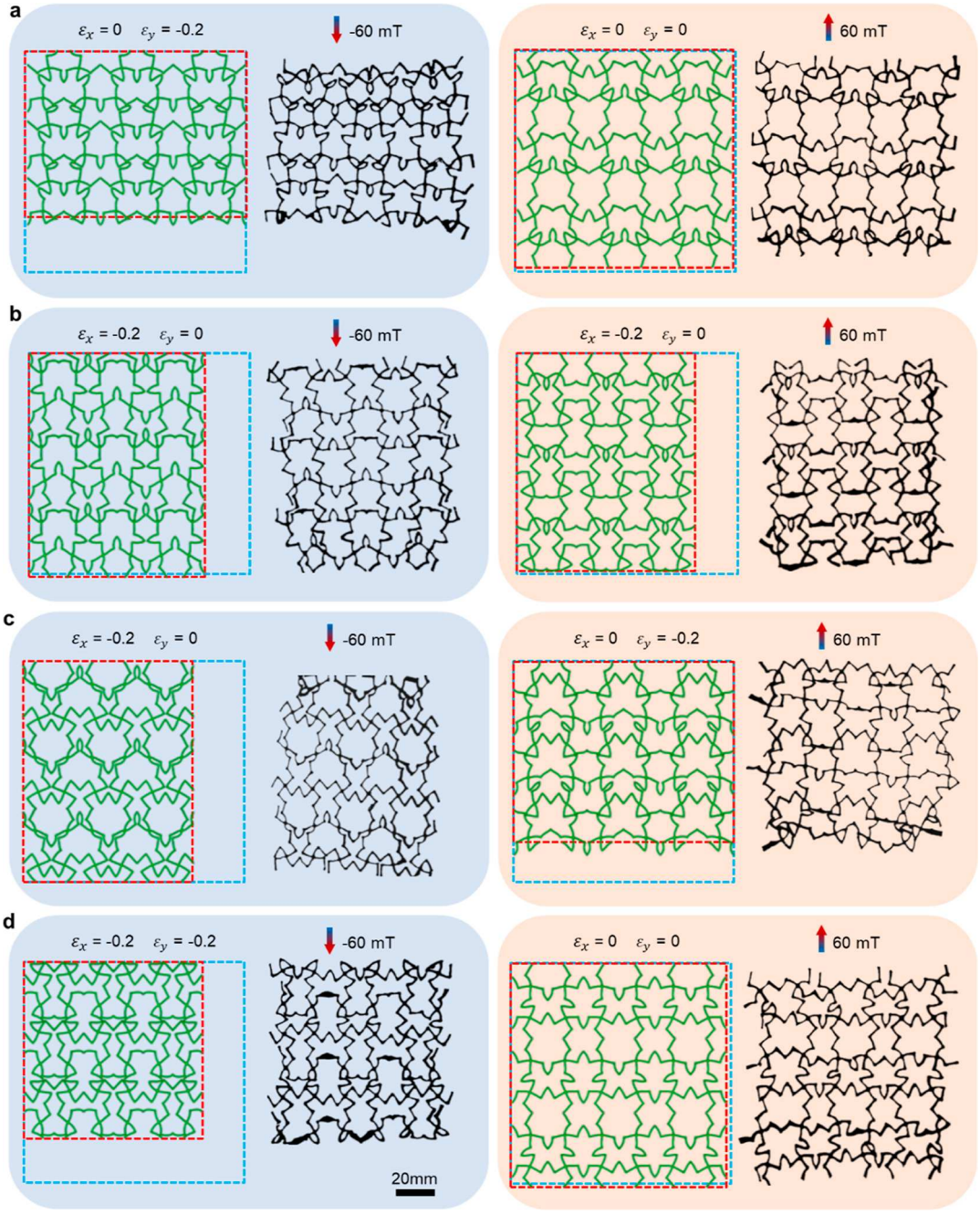

Figure 5. Comparisons between FEA and experiments using 3 × 3 arrays of the designed M-distributions in Figure 4. (a) Example from Type A for the control of the uniaxial strain with zero Poisson's ratio under one magnetic field and zero strain under the opposite magnetic field. (b) Example from Type B for the control of the uniaxial strain with zero Poisson's ratio under two opposite magnetic fields on the same axis. (c) Example from Type C for the control of the uniaxial strain with zero Poisson's ratio under two opposite magnetic fields on different axes. (d) Example from Type D for the control of the biaxial strain with negative Poisson's ratio under one magnetic field and zero strain under the opposite magnetic field.

can be seen that the strains either from DABC-ResNet or FEA match well with the target strains, and the experimental deformations are in line with the FEA, proving that the presented inverse design framework is effective and reliable. It is noteworthy that the experimental unit cell deformations in Figure 4 are cropped from the metamaterial arrays of 3 × 3 unit cells, as shown in Figure 5. Note that because the periodic boundary condition is breached on the edges of the array in the experiment, only the unit cell at the center of the array is used for the comparison with the FEA results, as shown in Figure 4. The details of all examples of Type A to Type D can be found in Figures S3−S6 in Supporting Information, demonstrating the wide tunability of the magneto-mechanical metamaterials. Type A (Figure S3) demonstrates the control of different degrees of strain. Type B and Type C (Figures S4 and S5) show independent control of uniaxial strain under both magnetic field directions, and Type D (Figure S6) shows different Poisson's ratios.

Figure 6 shows the examples from Type E to Type G of target strains. Two representative examples are selected from each type, demonstrating the wide tunability of deformation. Type E (Figure 6a,b) aims at the control of the biaxial strain with

https://doi.org/10.1021/acsami.2c09052
ACS Appl. Mater. Interfaces XXXX, XXX, XXX−XXX

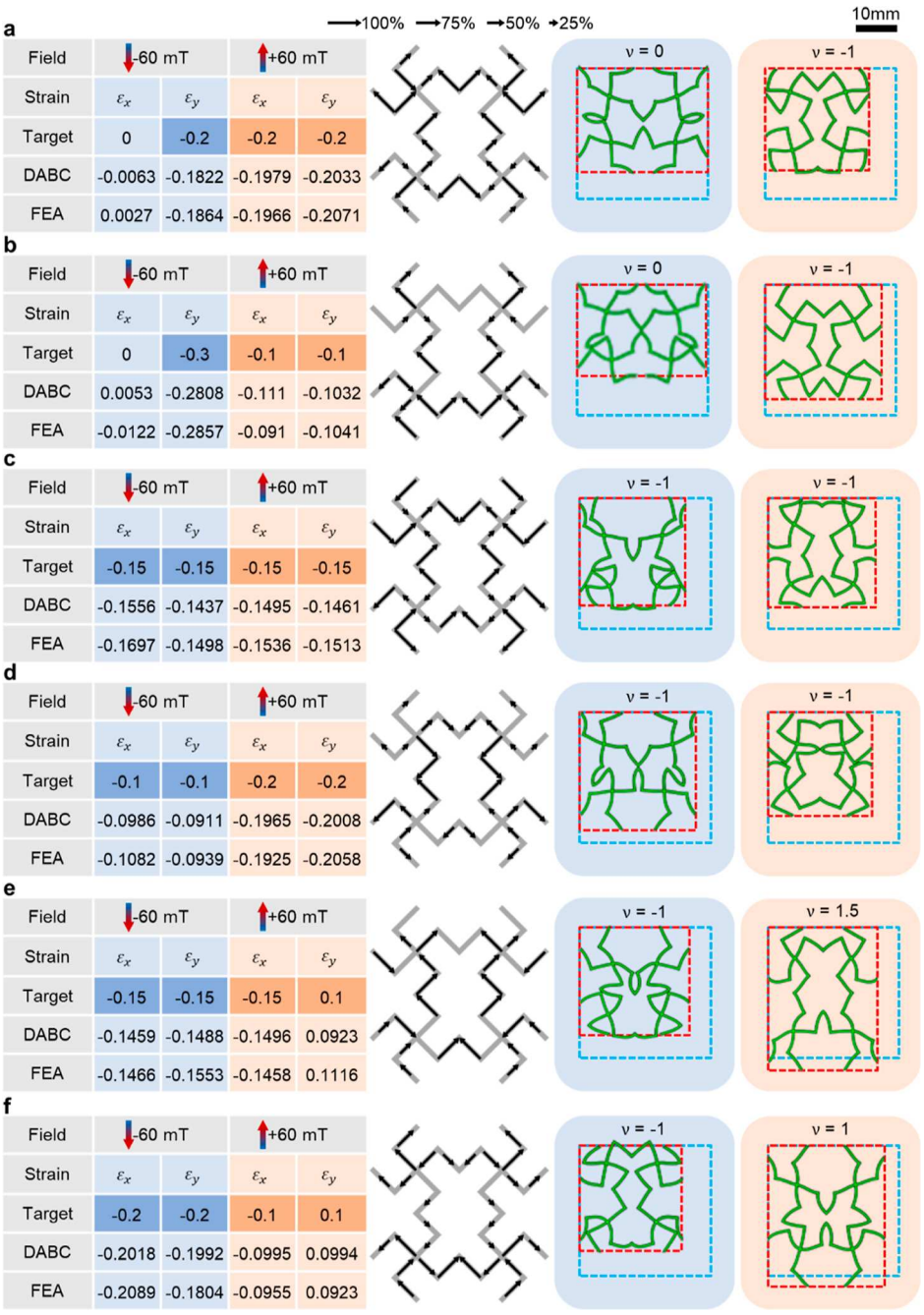

Figure 6. Examples of designed M-distributions and FEA results from Type E to Type G of target strains for deformation control. (a,b) Examples from Type E for the control of the biaxial strain with negative Poisson's ratio under one magnetic field and the uniaxial strain with zero Poisson's ratio under the opposite magnetic field. (c,d) Examples from Type F for the control of the biaxial strain with negative Poisson's ratio under two opposite magnetic fields. (e,f) Examples from Type G for the control of the biaxial strain with negative Poisson's ratio under one opposite magnetic field and the biaxial strain with positive Poisson's ratio under the opposite magnetic field.

negative Poisson's ratio under one magnetic field and the uniaxial strain with zero Poisson's ratio under the opposite magnetic field. Type F (Figure 6c,d) is for the control of the biaxial strain with negative Poisson's ratio under two opposite magnetic fields. Type G (Figure 6e,f) focuses on the control of the biaxial strain with negative Poisson's ratio under one opposite magnetic field and the biaxial strain with positive Poisson's ratio under the opposite magnetic field. The details of all examples of Type E to Type G are shown in Figures S7−S9 in Supporting Information. Such broad tunability and designability can be the cornerstone for future research, such as assembling different unit cells to realize sophisticated deformation for more advanced functions.

CONCLUSIONS

In this paper, we develop a deep-learning accelerated framework for the on-demand design of a type of magneto-mechanical metamaterials that can satisfy specific target deformation by enforcing strains. First, a deep learning model based on convolutional neural networks, ResNet, is trained to replace the time-consuming FEA to predict the deformation of the magneto-mechanical metamaterials under both downward and

https://doi.org/10.1021/acsami.2c09052
ACS Appl. Mater. Interfaces XXXX, XXX, XXX−XXX

upward external magnetic fields. Then, a heuristic optimization algorithm of strong global search ability, DABC, employs the trained ResNet as the forward solver to inversely design the unit cell M-distribution of the magneto-mechanical metamaterials. We demonstrate the wide deformation tunability of the magneto-mechanical metamaterials using various combinations of targeted uniaxial/biaxial global strains under both directions of magnetic fields. The accuracy, effectiveness, and reliability of the DABC-ResNet framework are proved by FEA and experimental results. The proposed on-demand design framework opens avenues for metamaterial designs. With 3D printing techniques, the proposed framework will enable the multifunctionality of the metamaterial for more advanced control of deformation, stiffness, acoustic band gap, electromagnetic property, and so on.

MATERIALS AND METHODS

FEA of Magneto-Mechanical Metamaterials. A user-defined eight-node linear hexahedral element subroutine is applied in ABAQUS (Dassault System) to predict the responses of the magnetic-responsive soft materials following an incompressible hyperelastic constitutive model.[29] The magnetic moment densities, shear modulus, and external magnetic field intensities are 70 kA·m^{-1}, 300 kPa, and 60 mT, respectively. In this work, periodic boundary conditions are applied to the unit cell to predict the deformation of a large array.

Ink Formulation and Preparation for 3D Printing. The ink for DIW has embedded neodymium-iron-boron (NdFeB) microparticles with an average size of 5 μm (Magnequench Co., Ltd.) and a silicone-based resin. The resin is composed of SE1700 base (Dow Corning Corp.), SE1700 curing agent (Dow Corning Corp.), and Ecoflex 00-30 Part B (Smooth-on Inc.) with a volume ratio of 1:2:0.1 plus 2 wt % fumed silica nanoparticles with an average size of 20 nm (Sigma-Aldrich) with respect to the Ecoflex 00-30 Part B. First, SE1700 base and Ecoflex 00-30 Part B are mixed at 2000 rpm for 1 min using a centrifugal mixer (AR-100, Thinky Inc.). Next, 77.5 vol % NdFeB particles with respect to the SE1700 base are added to the earlier mixture and mixed at 2000 rpm for 2 min plus defoaming at 2200 rpm for 3 min. Then, the SE1700 curing agent is added and mixed at 2000 rpm for 1 min, and the ink is transferred into a 10 mL syringe barrel (Nordson EFD) and defoamed in the mixer at 2200 rpm for 3 min plus mixing at 2000 rpm for 2 min. Finally, the ink is magnetized by a 1.5 T impulse magnetic field generated by an in-house built magnetizer. After installing the printing nozzle of 410 μm inner diameter (SmoothFlow Tapered Tips, Nordson EFD), the syringe barrel filled with the magnetized composite ink is mounted to a customized gantry 3D printer (Aerotech). A customized Python script converts the designed M-distribution to the G-codes for printing. Then, the printed magneto-mechanical metamaterials are cured at 80 °C for 36 h. The fabrication process demonstrates good repeatability, owing to the stable and reliable property of the printing ink. The solidified magnetic composite also shows pure elastic behavior with reproducible mechanical properties.

Experimental Setup for Magnetic Actuation. The magneto-mechanical metamaterials are actuated by the one-dimensional magnetic field generated from a set of single-axis Helmholtz coils. To prevent out-of-plane deformation and reduce friction in the experiments, the metamaterials are placed in an acrylic water tank and are covered by a supported acrylic plate. To further reduce the friction, the magneto-mechanical metamaterial arrays, acrylic water tank, and acrylic cover plate are spray-coated with a layer of WD-40 Specialist silicone lubricant (WD-40 Company). These efforts effectively increase the repeatability of the magnetic actuation.

ASSOCIATED CONTENT

Supporting Information

The Supporting Information is available free of charge at https://pubs.acs.org/doi/10.1021/acsami.2c09052.

Data augmentation using symmetry; average operation of ResNet predictions; ResNet computational time; equations of DABC algorithm; scatter plots of the strains from the best-trained ResNet using a batch size of 70; and designed M-distributions and FEA results of Type A to Type G target strains (PDF)

AUTHOR INFORMATION

Corresponding Author

Ruike Renee Zhao − *Department of Mechanical Engineering, Stanford University, Stanford, California 94305, United States;* orcid.org/0000-0002-9292-5267; Email: rrzhao@stanford.edu

Authors

Chunping Ma − *Department of Mechanical and Aerospace Engineering, The Ohio State University, Columbus, Ohio 43210, United States*

Yilong Chang − *Department of Mechanical Engineering, Stanford University, Stanford, California 94305, United States*

Shuai Wu − *Department of Mechanical Engineering, Stanford University, Stanford, California 94305, United States*

Complete contact information is available at: https://pubs.acs.org/10.1021/acsami.2c09052

Author Contributions

C.M. and Y.C. contributed equally to this work. R.R.Z. designed research and supervised the study. C.M. performed the FE simulations and developed the design framework. Y.C., C.M., and S.W. performed the experiments. C.M., Y.C., S.W., and R.R.Z. wrote the manuscript.

Notes

The authors declare no competing financial interest.

ACKNOWLEDGMENTS

C.M., Y.C., S.W., and R.R.Z. acknowledge support from the National Science Foundation (NSF) Career Award CMMI-2145601 and NSF Award CMMI-2142789.

REFERENCES

(1) Lv, C.; Krishnaraju, D.; Konjevod, G.; Yu, H.; Jiang, H. Origami Based Mechanical Metamaterials. *Sci. Rep.* **2014**, *4*, 5979.

(2) Li, T.; Chen, Y.; Hu, X.; Li, Y.; Wang, L. Exploiting Negative Poisson's Ratio to Design 3D-Printed Composites with Enhanced Mechanical Properties. *Mater. Des.* **2018**, *142*, 247−258.

(3) Wang, P.; Casadei, F.; Shan, S.; Weaver, J. C.; Bertoldi, K. Harnessing Buckling to Design Tunable Locally Resonant Acoustic Metamaterials. *Phys. Rev. Lett.* **2014**, *113*, 014301.

(4) Wang, Y.; Yousefzadeh, B.; Chen, H.; Nassar, H.; Huang, G.; Daraio, C. Observation of Nonreciprocal Wave Propagation in a Dynamic Phononic Lattice. *Phys. Rev. Lett.* **2018**, *121*, 194301.

(5) Xu, X.; Wu, Q.; Pang, Y.; Cao, Y.; Fang, Y.; Huang, G.; Cao, C. Multifunctional Metamaterials for Energy Harvesting and Vibration Control. *Adv. Funct. Mater.* **2022**, *32*, 2107896.

(6) Zhang, Z.; Song, B.; Yao, Y.; Zhang, L.; Wang, X.; Fan, J.; Shi, Y. Bioinspired, Simulation-Guided Design of Polyhedron Metamaterial for Simultaneously Efficient Heat Dissipation and Energy Absorption. *Adv. Mater. Technol.* **2022**, 2200076.

(7) Phan, T.; Sell, D.; Wang, E. W.; Doshay, S.; Edee, K.; Yang, J.; Fan, J. A. High-Efficiency, Large-Area, Topology-Optimized Metasurfaces. *Light: Sci. Appl.* **2019**, *8*, 48.

(8) Wu, S.; Eichenberger, J.; Dai, J.; Chang, Y.; Ghalichechian, N.; Zhao, R. R. Magnetically Acutated Reconfigurable Metamaterials as Conformal Electromagnetic Filters. *Adv. Intell. Syst.* **2022**, 2200106.

(9) Paulose, J.; Meeussen, A. S.; Vitelli, V. Selective Buckling via States of Self-Stress in Topological Metamaterials. *Proc. Natl. Acad. Sci. U.S.A.* **2015**, *112*, 7639−7644.
(10) Chen, Y.; Li, T.; Scarpa, F.; Wang, L. Lattice Metamaterials with Mechanically Tunable Poisson's Ratio for Vibration Control. *Phys. Rev. Appl.* **2017**, *7*, 024012.
(11) Zhai, Z.; Wang, Y.; Jiang, H. Origami-Inspired, on-Demand Deployable and Collapsible Mechanical Metamaterials with Tunable Stiffness. *Proc. Natl. Acad. Sci. U.S.A.* **2018**, *115*, 2032−2037.
(12) Ding, Z.; Yuan, C.; Peng, X.; Wang, T.; Qi, H. J.; Dunn, M. L. Direct 4D Printing via Active Composite Materials. *Sci. Adv.* **2017**, *3*, No. e1602890.
(13) Boley, J. W.; van Rees, W. M.; Lissandrello, C.; Horenstein, M. N.; Truby, R. L.; Kotikian, A.; Lewis, J. A.; Mahadevan, L. Shape-Shifting Structured Lattices via Multimaterial 4D Printing. *Proc. Natl. Acad. Sci. U.S.A.* **2019**, *116*, 20856−20862.
(14) Deng, H.; Xu, X.; Zhang, C.; Su, J.-W.; Huang, G.; Lin, J. Deterministic Self-Morphing of Soft-Stiff Hybridized Polymeric Films for Acoustic Metamaterials. *ACS Appl. Mater. Interfaces* **2020**, *12*, 13378−13385.
(15) Liu, Y.; Shaw, B.; Dickey, M. D.; Genzer, J. Sequential Self-Folding of Polymer Sheets. *Sci. Adv.* **2017**, *3*, No. e1602417.
(16) Wang, Y.; Dang, A.; Zhang, Z.; Yin, R.; Gao, Y.; Feng, L.; Yang, S. Repeatable and Reprogrammable Shape Morphing from Photo-responsive Gold Nanorod/Liquid Crystal Elastomers. *Adv. Mater.* **2020**, *32*, 2004270.
(17) Jackson, J. A.; Messner, M. C.; Dudukovic, N. A.; Smith, W. L.; Bekker, L.; Moran, B.; Golobic, A. M.; Pascall, A. J.; Duoss, E. B.; Loh, K. J.; Spadaccini, C. M. Field Responsive Mechanical Metamaterials. *Sci. Adv.* **2018**, *4*, No. eaau6419.
(18) Alapan, Y.; Karacakol, A. C.; Guzelhan, S. N.; Isik, I.; Sitti, M. Reprogrammable Shape Morphing of Magnetic Soft Machines. *Sci. Adv.* **2020**, *6*, No. eabc6414.
(19) Ze, Q.; Kuang, X.; Wu, S.; Wong, J.; Montgomery, S. M.; Zhang, R.; Kovitz, J. M.; Yang, F.; Qi, H. J.; Zhao, R. Magnetic Shape Memory Polymers with Integrated Multifunctional Shape Manipulation. *Adv. Mater.* **2020**, *32*, 1906657.
(20) Ren, Z.; Hu, W.; Dong, X.; Sitti, M. Multi-Functional Soft-Bodied Jellyfish-like Swimming. *Nat. Commun.* **2019**, *10*, 2703.
(21) Wu, S.; Ze, Q.; Dai, J.; Udipi, N.; Paulino, G. H.; Zhao, R. Stretchable Origami Robotic Arm with Omnidirectional Bending and Twisting. *Proc. Natl. Acad. Sci. U.S.A.* **2021**, *118*, No. e2110023118.
(22) Hu, W.; Lum, G. Z.; Mastrangeli, M.; Sitti, M. Small-Scale Soft-Bodied Robot with Multimodal Locomotion. *Nature* **2018**, *554*, 81−85.
(23) Kim, Y.; Parada, G. A.; Liu, S.; Zhao, X. Ferromagnetic Soft Continuum Robots. *Sci. Robot.* **2019**, *4*, No. eaax7329.
(24) Kim, Y.; Yuk, H.; Zhao, R.; Chester, S. A.; Zhao, X. Printing Ferromagnetic Domains for Untethered Fast-Transforming Soft Materials. *Nature* **2018**, *558*, 274−279.
(25) Wu, S.; Ze, Q.; Zhang, R.; Hu, N.; Cheng, Y.; Yang, F.; Zhao, R. Symmetry-Breaking Actuation Mechanism for Soft Robotics and Active Metamaterials. *ACS Appl. Mater. Interfaces* **2019**, *11*, 41649−41658.
(26) Cui, J.; Huang, T.-Y.; Luo, Z.; Testa, P.; Gu, H.; Chen, X.-Z.; Nelson, B. J.; Heyderman, L. J. Nanomagnetic Encoding of Shape-Morphing Micromachines. *Nature* **2019**, *575*, 164−168.
(27) Montgomery, S. M.; Wu, S.; Kuang, X.; Armstrong, C. D.; Zemelka, C.; Ze, Q.; Zhang, R.; Zhao, R.; Qi, H. J. Magneto-Mechanical Metamaterials with Widely Tunable Mechanical Properties and Acoustic Bandgaps. *Adv. Funct. Mater.* **2020**, *31*, 2005319.
(28) Ma, C.; Wu, S.; Ze, Q.; Kuang, X.; Zhang, R.; Qi, H. J.; Zhao, R. Magnetic Multimaterial Printing for Multimodal Shape Transformation with Tunable Properties and Shiftable Mechanical Behaviors. *ACS Appl. Mater. Interfaces* **2020**, *13*, 12639.
(29) Zhao, R.; Kim, Y.; Chester, S. A.; Sharma, P.; Zhao, X. Mechanics of Hard-Magnetic Soft Materials. *J. Mech. Phys. Solids* **2019**, *124*, 244−263.
(30) Wu, S.; Hamel, C. M.; Ze, Q.; Yang, F.; Qi, H. J.; Zhao, R. Evolutionary Algorithm-Guided Voxel-Encoding Printing of Functional Hard-Magnetic Soft Active Materials. *Adv. Intell. Syst.* **2020**, *2*, 2000060.
(31) Abueidda, D. W.; Almasri, M.; Ammourah, R.; Ravaioli, U.; Jasiuk, I. M.; Sobh, N. A. Prediction and Optimization of Mechanical Properties of Composites Using Convolutional Neural Networks. *Compos. Struct.* **2019**, *227*, 111264.
(32) Stern, M.; Arinze, C.; Perez, L.; Palmer, S. E.; Murugan, A. Supervised Learning through Physical Changes in a Mechanical System. *Proc. Natl. Acad. Sci. U.S.A.* **2020**, *117*, 14843−14850.
(33) Abueidda, D. W.; Koric, S.; Sobh, N. A.; Sehitoglu, H. Deep Learning for Plasticity and Thermo-Viscoplasticity. *Int. J. Plast.* **2021**, *136*, 102852.
(34) Sun, X.; Yue, L.; Yu, L.; Shao, H.; Peng, X.; Zhou, K.; Demoly, F.; Zhao, R.; Qi, H. J. Machine Learning-Evolutionary Algorithm Enabled Design for 4D-Printed Active Composite Structures. *Adv. Funct. Mater.* **2022**, *32*, 2109805.
(35) Gu, G. X.; Chen, C.-T.; Buehler, M. J. De Novo Composite Design Based on Machine Learning Algorithm. *Extreme Mech. Lett.* **2018**, *18*, 19−28.
(36) Ma, W.; Cheng, F.; Xu, Y.; Wen, Q.; Liu, Y. Probabilistic Representation and Inverse Design of Metamaterials Based on a Deep Generative Model with Semi-Supervised Learning Strategy. *Adv. Mater.* **2019**, *31*, 1901111.
(37) Kumar, S.; Tan, S.; Zheng, L.; Kochmann, D. M. Inverse-Designed Spinodoid Metamaterials. *npj Comput. Mater.* **2020**, *6*, 1−10.
(38) Mao, Y.; He, Q.; Zhao, X. Designing Complex Architectured Materials with Generative Adversarial Networks. *Sci. Adv.* **2020**, *6*, No. eaaz4169.
(39) Kollmann, H. T.; Abueidda, D. W.; Koric, S.; Guleryuz, E.; Sobh, N. A. Deep Learning for Topology Optimization of 2D Metamaterials. *Mater. Des.* **2020**, *196*, 109098.
(40) Ioffe, S.; Szegedy, C. Batch Normalization: Accelerating Deep Network Training by Reducing Internal Covariate Shift. *Proceedings of the 32nd International Conference on Machine Learning*; PMLR, 2015; pp 448−456.
(41) He, K.; Zhang, X.; Ren, S.; Sun, J. Deep Residual Learning for Image Recognition. *2016 IEEE Conference on Computer Vision and Pattern Recognition (CVPR)*; IEEE: Las Vegas, NV, USA, 2016; pp 770−778.
(42) Zhao, Y.; Cao, X.; Gao, J.; Sun, Y.; Yang, H.; Liu, X.; Zhou, Y.; Han, T.; Chen, W. Broadband Diffusion Metasurface Based on a Single Anisotropic Element and Optimized by the Simulated Annealing Algorithm. *Sci. Rep.* **2016**, *6*, 23896.
(43) Kitai, K.; Guo, J.; Ju, S.; Tanaka, S.; Tsuda, K.; Shiomi, J.; Tamura, R. Designing Metamaterials with Quantum Annealing and Factorization Machines. *Phys. Rev. Res.* **2020**, *2*, 013319.
(44) Garland, A. P.; White, B. C.; Jensen, S. C.; Boyce, B. L. Pragmatic Generative Optimization of Novel Structural Lattice Metamaterials with Machine Learning. *Mater. Des.* **2021**, *203*, 109632.
(45) Chen, P. Y.; Chen, C. H.; Wang, H.; Tsai, J. H.; Ni, W. X. Synthesis Design of Artificial Magnetic Metamaterials Using a Genetic Algorithm. *Opt. Express* **2008**, *16*, 12806−12818.
(46) Hamel, C. M.; Roach, D. J.; Long, K. N.; Demoly, F.; Dunn, M. L.; Qi, H. J. Machine-Learning Based Design of Active Composite Structures for 4D Printing. *Smart Mater. Struct.* **2019**, *28*, 065005.
(47) Sun, H.; Waisman, H.; Betti, R. A Multiscale Flaw Detection Algorithm Based on XFEM. *Int. J. Numer. Methods Eng.* **2014**, *100*, 477−503.
(48) Ma, C.; Yu, T.; Van Lich, L.; Quoc Bui, T. An Effective Computational Approach Based on XFEM and a Novel Three-Step Detection Algorithm for Multiple Complex Flaw Clusters. *Comput. Struct.* **2017**, *193*, 207−225.
(49) Ma, C.; Yu, T.; Van Lich, L.; Thanh-Tung, N.; Bui, T. Q. Detection of Multiple Complicated Flaw Clusters by Dynamic Variable-Node XFEM with a Three-Step Detection Algorithm. *Eur. J. Mech. Solid.* **2020**, *82*, 103980.
(50) Abadi, M.; Agarwal, A.; Barham, P.; Brevdo, E.; Chen, Z.; Citro, C.; Corrado, G. S.; Davis, A.; Dean, J.; Devin, M.; Ghemawat, S.; Goodfellow, I.; Harp, A.; Irving, G.; Isard, M.; Jia, Y.; Jozefowicz, R.;

https://doi.org/10.1021/acsami.2c09052
ACS Appl. Mater. Interfaces XXXX, XXX, XXX−XXX

Kaiser, L.; Kudlur, M.; Levenberg, J.; Mane, D.; Monga, R.; Moore, S.; Murray, D.; Olah, C.; Schuster, M.; Shlens, J.; Steiner, B.; Sutskever, I.; Talwar, K.; Tucker, P.; Vanhoucke, V.; Vasudevan, V.; Viegas, F.; Vinyals, O.; Warden, P.; Wattenberg, M.; Wicke, M.; Yu, Y.; Zheng, X. TensorFlow: Large-Scale Machine Learning on Heterogeneous Distributed Systems. **2016**, arXiv:1603.04467v2.

(51) Kingma, D. P.; Ba, J. Adam: A Method for Stochastic Optimization. arXiv January 29, **2017**, arXiv:1412.6980.

(52) Hinton, G. E. A Practical Guide to Training Restricted Boltzmann Machines. In *Neural Networks: Tricks of the Trade*, 2nd ed.; Montavon, G., Orr, G. B., Müller, K.-R., Eds.; Lecture Notes in Computer Science; Springer: Berlin, Heidelberg, 2012; pp 599−619.

https://doi.org/10.1021/acsami.2c09052
ACS Appl. Mater. Interfaces XXXX, XXX, XXX−XXX